

Broadband terahertz dispersion control in hybrid waveguides

TOBIAS FOBBE,^{1,2,*} SERGEJ MARKMANN,¹ FELIX FOBBE,⁴ NEGAR HEKMAT,¹ HANOND NONG,¹ SHOYON PAL,^{1,2} PATRICK BALZERWOSKI,³ JANNE SAVOLAINEN,³ MARTINA HAVENITH,³ ANDREAS D. WIECK,² AND NATHAN JUKAM^{1,5}

¹AG Terahertz Spektroskopie und Technologie, Ruhr-Universität Bochum, D-44780 Bochum, Germany

²Lehrstuhl für Angewandte Festkörperphysik, Ruhr-Universität Bochum, D-44780 Bochum, Germany

³Lehrstuhl für Physikalische Chemie II, Ruhr-Universität Bochum, D-44780 Bochum, Germany

⁴Lehrstuhl für Experimentelle Physik 2, Technische Universität Dortmund, D-44227 Dortmund, Germany

⁵nathan.jukam@rub.de

*tobias.fobbe@rub.de

Abstract: Dispersion control is a key objective in the field of photonics and spectroscopy, since it enhances non-linear effects by both enabling phase matching and offering slow light generation. In addition, it is essential for frequency comb generation, which requires a phase-lock mechanism that is provided by broadband compensation of group velocity dispersion (GVD). At optical frequencies, there are several well-established concepts for dispersion control such as prism or grating pairs. However, terahertz dispersion control is still a challenge, thus hindering further progress in the field of terahertz science and technology. In this work, we present a hybrid waveguide with both broadband, tuneable positive and more than octave-spanning negative terahertz GVD on the order of 10^{-22} s²/m, which is suitable for either intra- or extra cavity operation. This new terahertz device will enable ultra-short pulse compression, allow soliton propagation, improve frequency comb operation and foster the development of novel non-linear applications.

© 2016 Optical Society of America

OCIS codes: (230.7370) Waveguides; (130.2035) Dispersion compensation devices; (300.6495) Spectroscopy, terahertz.

References and links

1. G. Villares, A. Hugi, S. Blaser, and J. Faist, "Dual-comb spectroscopy based on quantum-cascade-laser frequency combs," *Nat. Commun.* **5**, 5192 (2014).
2. F. Keilmann, C. Gohle, and R. Holzwarth, "Time-domain mid-infrared frequency-comb spectrometer," *Opt. Lett.* **29**(13), 1542–1544 (2004).
3. S. Schiller, "Spectrometry with frequency combs," *Opt. Lett.* **27**(9), 766–768 (2002).
4. T. Udem, R. Holzwarth, and T. W. Hänsch, "Optical frequency metrology," *Nature* **416**(6877), 233–237 (2002).
5. A. Schliesser, N. Picqué, and T. Hänsch, "Mid-infrared frequency combs," *Nat. Photonics* **6**(7), 440–449 (2012).
6. A. Hugi, G. Villares, S. Blaser, H. C. Liu, and J. Faist, "Mid-infrared frequency comb based on a quantum cascade laser," *Nature* **492**(7428), 229–233 (2012).
7. M. D. Settle, R. J. Engelen, M. Salib, A. Michaeli, L. Kuipers, and T. F. Krauss, "Flatband slow light in photonic crystals featuring spatial pulse compression and terahertz bandwidth," *Opt. Express* **15**(1), 219–226 (2007).
8. L. Thévenaz, "Slow and fast light in optical fibres," *Nat. Photonics* **2**(8), 474–481 (2008).
9. T. Baba, "Slow light in photonic crystals," *Nat. Photonics* **2**(8), 465–473 (2008).
10. Y. A. Vlasov, M. O'Boyle, H. F. Hamann, and S. J. McNab, "Active control of slow light on a chip with photonic crystal waveguides," *Nature* **438**(7064), 65–69 (2005).
11. U. Keller, "Recent developments in compact ultrafast lasers," *Nature* **424**(6950), 831–838 (2003).
12. S. Barbieri, M. Ravano, P. Gellie, G. Santarelli, C. Manquest, C. Sirtori, S. Khanna, E. H. Linfield, and A. G. Davies, "Coherent sampling of active mode-locked terahertz quantum cascade lasers and frequency synthesis," *Nat. Photonics* **5**(5), 306–313 (2011).
13. D. G. Ouzounov, F. R. Ahmad, D. Müller, N. Venkataraman, M. T. Gallagher, M. G. Thomas, J. Silcox, K. W. Koch, and A. L. Gaeta, "Generation of megawatt optical solitons in hollow-core photonic band-gap fibers," *Science* **301**(5640), 1702–1704 (2003).
14. P. Russell, "Photonic crystal fibers," *Science* **299**(5605), 358–362 (2003).

15. J. C. Knight, "Photonic crystal fibres," *Nature* **424**(6950), 847–851 (2003).
16. J. G. Rivas, M. Kuttge, P. H. Bolivar, H. Kurz, and J. A. Sánchez-Gil, "Propagation of surface plasmon polaritons on semiconductor gratings," *Phys. Rev. Lett.* **93**(25), 256804 (2004).
17. P. Maker, R. Terhune, M. Nisenoff, and C. Savage, "Effects of dispersion and focusing on the production of optical harmonics," *Phys. Rev. Lett.* **8**(1), 21–22 (1962).
18. R. L. Fork, O. E. Martinez, and J. P. Gordon, "Negative dispersion using pairs of prisms," *Opt. Lett.* **9**(5), 150–152 (1984).
19. O. Martinez, "3000 times grating compressor with positive group velocity dispersion: application to fiber compensation in 1.3–1.6 μm region," *IEEE J. Quantum Electron.* **23**(1), 59–64 (1987).
20. F. X. Kärtner, U. Morgner, R. Ell, T. Schibli, J. G. Fujimoto, E. P. Ippen, V. Scheuer, G. Angelow, and T. Tschudi, "Ultrabroadband double-chirped mirror pairs for generation of octave spectra," *J. Opt. Soc. Am. B* **18**(6), 882–885 (2001).
21. R. Szipöcs, C. Spielmann, F. Krausz, and K. Ferencz, "Chirped multilayer coatings for broadband dispersion control in femtosecond lasers," *Opt. Lett.* **19**(3), 201–203 (1994).
22. M. Strain and M. Sorel, "Design and fabrication of integrated chirped bragg gratings for on-chip dispersion control," *IEEE J. Quantum Electron.* **46**(5), 774–782 (2010).
23. B. Golubovic, R. R. Austin, M. K. Steiner-Shepard, M. K. Reed, S. A. Diddams, D. J. Jones, and A. G. Van Engen, "Double Gires-Tournois interferometer negative-dispersion mirrors for use in tunable mode-locked lasers," *Opt. Lett.* **25**(4), 275–277 (2000).
24. F. M. Mitschke and L. F. Mollenauer, "Ultrashort pulses from the soliton laser," *Opt. Lett.* **12**(6), 407–409 (1987).
25. S. V. Chernikov, D. J. Richardson, D. N. Payne, and E. M. Dianov, "Soliton pulse compression in dispersion-decreasing fiber," *Opt. Lett.* **18**(7), 476–478 (1993).
26. K. Saitoh, M. Koshiba, T. Hasegawa, and E. Sasaoka, "Chromatic dispersion control in photonic crystal fibers: application to ultra-flattened dispersion," *Opt. Express* **11**(8), 843–852 (2003).
27. D. Burghoff, T. Kao, N. Han, C. Chan, X. Cai, Y. Yang, D. Hayton, J. Gao, J. Reno, and Q. Hu, "Terahertz laser frequency combs," *Nat. Photonics* **8**(6), 462–467 (2014).
28. M. Rösch, G. Scalari, M. Beck, and J. Faist, "Octave-spanning semiconductor laser," *Nat. Photonics* **9**(1), 42–47 (2014).
29. M. S. Vitiello, G. Scalari, B. Williams, and P. De Natale, "Quantum cascade lasers: 20 years of challenges," *Opt. Express* **23**(4), 5167–5182 (2015).
30. G. Villares and J. Faist, "Quantum cascade laser combs: effects of modulation and dispersion," *Opt. Express* **23**(2), 1651–1669 (2015).
31. G. Scalari, C. Walther, M. Fischer, R. Terazzi, H. Beere, D. Ritchie, and J. Faist, "THz and sub-THz quantum cascade lasers," *Laser Photonics Rev.* **3**(1-2), 45–66 (2009).
32. T. Fobbe, H. Nong, R. Schott, S. Pal, S. Markmann, N. Hekmat, J. Zhu, Y. Han, L. Li, P. Dean, E. H. Linfield, A. G. Davies, A. D. Wieck, and N. Jukam, "Improving the out-coupling of a metal-metal terahertz frequency quantum cascade laser through integration of a hybrid mode section into the waveguide," *J. Infrar. Millim. THz Waves* **37**(5), 426–434 (2016).
33. A. C. Turner, C. Manolatu, B. S. Schmidt, M. Lipson, M. A. Foster, J. E. Sharping, and A. L. Gaeta, "Tailored anomalous group-velocity dispersion in silicon channel waveguides," *Opt. Express* **14**(10), 4357–4362 (2006).
34. L. Tong, J. Lou, and E. Mazur, "Single-mode guiding properties of subwavelength-diameter silica and silicon wire waveguides," *Opt. Express* **12**(6), 1025–1035 (2004).
35. H. Nong, S. Pal, S. Markmann, N. Hekmat, R. Mohandas, P. Dean, L. Li, E. H. Linfield, A. G. Davies, A. D. Wieck, and N. Jukam, "Narrow-band injection seeding of a terahertz frequency quantum cascade laser: Selection and suppression of longitudinal modes," *Appl. Phys. Lett.* **105**(11), 111113 (2014).
36. S. Pal, H. Nong, S. Markmann, N. Kukharchyk, S. Valentin, S. Scholz, A. Ludwig, C. Bock, U. Kunze, A. D. Wieck, and N. Jukam, "Ultrawide electrical tuning of light matter interaction in a high electron mobility transistor structure," *Sci. Rep.* **5**, 16812 (2015).
37. E. Wigner, "On the quantum correction for thermodynamic equilibrium," *Phys. Rev.* **40**(5), 749–759 (1932).
38. J. Ville, "Théorie et applications de la notion de signal analytique," *Cables Transm.* **2**, 61–74 (1948).
39. L. Cohen, *Time-frequency Analysis* (Prentice Hall PTR, 1995).
40. B. Williams, "Terahertz quantum-cascade lasers," *Nat. Photonics* **5**, 17–25 (2007).
41. J. Faist, F. Capasso, D. L. Sivco, C. Sirtori, A. L. Hutchinson, and A. Y. Cho, "Quantum cascade laser," *Science* **264**(5158), 553–556 (1994).
42. H. Han, H. Park, M. Cho, and J. Kim, "Terahertz pulse propagation in a plastic photonic crystal fiber," *Appl. Phys. Lett.* **80**(15), 2634–2636 (2002).
43. M. Cho, J. Kim, H. Park, Y. Han, K. Moon, E. Jung, and H. Han, "Highly birefringent terahertz polarization maintaining plastic photonic crystal fibers," *Opt. Express* **16**(1), 7–12 (2008).

1. Introduction

Traditionally, dispersion control plays a fundamental role both in optical industry and research, since it represents an essential ingredient to modern technology such as optical fibre communication, ultrafast mode-locked laser systems or non-linear applications. Optical

frequency combs, which have opened new avenues in high resolution infrared spectroscopy [1–3] and metrology [4], illustrate the meaningful role of dispersion compensation exemplarily. A frequency comb is a laser source that provides evenly spaced phase-locked modes [5], which requires a compensation of group velocity dispersion (GVD). Beyond GVD compensation for frequency comb generation [6], dispersion control offers great potential for slow light phenomena [7–10], ultra-short laser physics [11,12], photonic crystal fibres [13–15], sensitive spectroscopy [16], soliton generation [13] and improving the phase matching for the optimization of parametric processes [17]. In the optical regime there are several approaches established to achieve dispersion control that typically aim for compensation of a positive material GVD. More precisely, at optical frequencies GVD control is traditionally achieved by prism pairs [18], grating pairs [19], chirped mirrors [20,21], chirped Bragg gratings [22], Gires-Tournois interferometers [23], compression fibres [24,25] or photonic crystal fibres [26].

However at terahertz (THz) frequencies, only a limited advance towards dispersion control has been reported [27], even though signals in THz time domain spectroscopy are often degraded due to excessive dispersion and larger signals could be obtained via pulse compression. Recently, it has been shown that the generation of octave-spanning THz laser frequency combs is limited due to a lack of broadband dispersion management [28–30]. In addition, the field of non-linear THz optics is rapidly developing, but is still underdeveloped compared to its optical counterpart. Thus, completely new research fields such as THz soliton propagation and THz self-phase modulation in fibres could be envisaged, if THz dispersion control becomes accessible. Recognizing both, the innovative research based on dispersion control at optical frequencies and the unexplored potential in the THz regime, it becomes apparent that there is a strong need for THz dispersion control.

Here, we approach the challenge of providing THz dispersion control through integration of a dielectric-metal (DM) mode section into a common metal-metal (MM) waveguide [31], thus forming a hybrid waveguide. The DM mode is enabled by absence of the top metal layer of the MM-waveguide, incorporating a high index contrast between the core and the dielectric cladding, which could be air [32]. If the waveguide dimensions are shrunk, so that a portion of the mode resides both outside and inside the waveguide, strong waveguide dispersion can result in anomalous GVD [33,34]. The proposed hybrid waveguide provides full THz dispersion control featuring strong broadband positive and negative GVD, which is experimentally investigated by THz time domain spectroscopy and supported by both a theoretical model and a Wigner-Ville analysis. In addition, THz dispersion control could be implemented for both intra-cavity and external cavity applications. Furthermore, GVD tuning is achieved by varying the waveguide height or the refractive index of the top dielectric medium.

2. Experimental access to dispersion relation

2.1 Waveguide processing and THz time domain spectroscopy

A Si wafer with a resistivity > 1000 Ohms/cm has been evaporated with 20 nm Cr and 200 nm Au from both sides. A mask has been used to photo-lithographically generate the DM section of length l at the end of the waveguide. The samples were cleaved into 3.5 mm and 2 mm wide pieces. A MM and the hybrid waveguide were mounted by means of a flip-chip bonder on a sub-mount such that both facets of the waveguides terminate with the metallic sub-mount to prevent blocking the in- or out-coupling radiation. A sample holder with an Au-coated and cleaved leakage block on top of the waveguides is used to minimize the leakage signal. To improve the coupling efficiency the samples were positioned via an x,y,z -stage and a rotatory mount.

Laser power of 260 mW provided by a Ti:Sa laser with 80 fs pulse duration, 800 nm wavelength and a repetition rate of 80 MHz is used to excite a DC biased inter-digitated photoconductive antenna processed on a GaAs substrate. Two 90° off-axis parabolic mirrors

are used to collimate and couple the THz beam into the waveguides. The electric field component of the source is in the direction parallel to the optical table such that the fundamental TM_1 DM waveguide mode is excited. Two additional parabolic mirrors are used to collect the signal and focus it on a ZnTe detection crystal. Under purged conditions the generated THz signal is electro-optically detected by employing a birefringent 2 mm thick ZnTe crystal.

2.2 Calculation of dispersion relation

The GVD of the DM section is obtained from the time domain signals. For that purpose, a Fourier-transform of the waveguide signals is performed to extract the spectral phases $\phi_{L,l}^{\text{Hyb}}(\omega)$ and $\phi_{L,l}^{\text{MM}}(\omega)$ for the hybrid and the MM waveguide, where L is the total waveguide length and l denotes the length of the DM section. In order to determine the dispersion relation of the DM section, the net spectral phase of the DM section $\phi_l^{\text{DM}}(\omega)$ is obtained from:

$$\phi_l^{\text{DM}}(\omega) = \phi_{L,l}^{\text{Hyb}}(\omega) - \frac{L-l}{L} \phi_{L,l}^{\text{MM}}(\omega). \quad (1)$$

Employing fundamental relationships: $\phi_l^{\text{DM}}(\omega) = \beta(\omega)l + \omega t_0$ and $n_{\text{eff}}(\omega) = \frac{\beta(\omega)c}{\omega}$, the effective refractive index is calculated from

$$n_{\text{eff}}(\omega) = \frac{c}{l} \left(\frac{\phi_l^{\text{DM}}(\omega)}{\omega} - t_0 \right), \quad (2)$$

where c is the speed of light and the time t_0 denotes a constant that describes the position of the dispersion relation n_{eff} with respect to the y -axis.

3. Results and discussion

3.1 Theoretical model and characterization of the DM section

The dielectric-metal section shown in Fig. 1(a) is described as a three-layer system in the manner of a two-dimensional electromagnetic plane wave problem. We assume plane waves in the y - z plane and write for the electric and magnetic field:

$$(E, H) = (E_m, H_m)(z, \beta_m) \exp(i(\omega t - \beta_m y)). \quad (3)$$

Here, β_m denotes the propagation constant for mode m , ω the angular frequency, t the time, y the propagation and z the growth direction. According to the polarization selection rule of intersubband transitions, QCLs only provide gain for TM modes where $(E_y, E_z, H_x) \neq 0$. Consequently, we consider the H_x -field component that is given by:

$$H_{x,m} = \begin{cases} C \exp(-r(\beta_m)z) & z > 0 \\ E \sin(h(\beta_m)z) + F \cos(h(\beta_m)z) & 0 < z < d \\ D \exp(q(\beta_m)z) & z < 0. \end{cases} \quad (4)$$

The β_m -dependent wave vector amplitudes of the three layer system are given in terms of the dielectric permittivity of the metal ϵ_m , and the dielectric permittivity of the two dielectric layers ϵ_1 and ϵ_2 :

$$\begin{aligned}
 r(\beta_m) &= \sqrt{\beta_m^2 - \varepsilon_2 \frac{\omega^2}{c^2}}, \\
 h(\beta_m) &= \sqrt{\varepsilon_1 \frac{\omega^2}{c^2} - \beta_m^2}, \\
 q(\beta_m) &= \sqrt{\beta_m^2 - \varepsilon_m \frac{\omega^2}{c^2}}.
 \end{aligned} \tag{5}$$

The metallic dielectric function is given by $\varepsilon_m = 1 - \frac{\omega_p^2 \tau^2}{1 + \omega^2 \tau^2} + i \frac{\omega_p^2 \tau / \omega}{1 + \omega^2 \tau^2}$, where the plasma frequency of gold is $\omega_p = 1.36 \times 10^{16}$ Hz and the scattering relaxation time is $\tau = 10$ fs. The ansatz (Eq. (3)) with the mode profile (Eq. (4)) fulfills the Maxwell equation and has to match the boundary conditions, e.g. the continuity of $H_{x,m}$ and $\frac{1}{\varepsilon_i} \frac{dH_{x,m}}{dx}$ boundaries $z = 0$ and $z = d$, resulting in a set of four equations. Solving this system leads to a complex transcendental equation for β_m :

$$\tan(h(\beta_m)d) = \frac{r(\beta_m)h(\beta_m)\varepsilon_1\varepsilon_m + h(\beta_m)q(\beta_m)\varepsilon_1\varepsilon_2}{h(\beta_m)^2\varepsilon_2\varepsilon_m - q(\beta_m)r(\beta_m)\varepsilon_1^2}. \tag{6}$$

In fact, solving Eq. (6) is not straight forward, since typical commercial software algorithms typically fail to find the correct solution. However, neglecting the imaginary part of ε_m turns out to be a very good approximation and significantly simplifies the conditional equation for β_m . Finally the real propagation constant for a given frequency is obtained graphically or numerically. For confined modes the propagation constant lies in the interval $\sqrt{\varepsilon_2} \frac{\omega}{c} < \beta_m < \sqrt{\varepsilon_1} \frac{\omega}{c}$. The GVD is obtained as the second derivative with respect to the propagation constant, i.e.:

$$GVD \equiv \frac{d^2 \beta_m}{d\omega^2}. \tag{7}$$

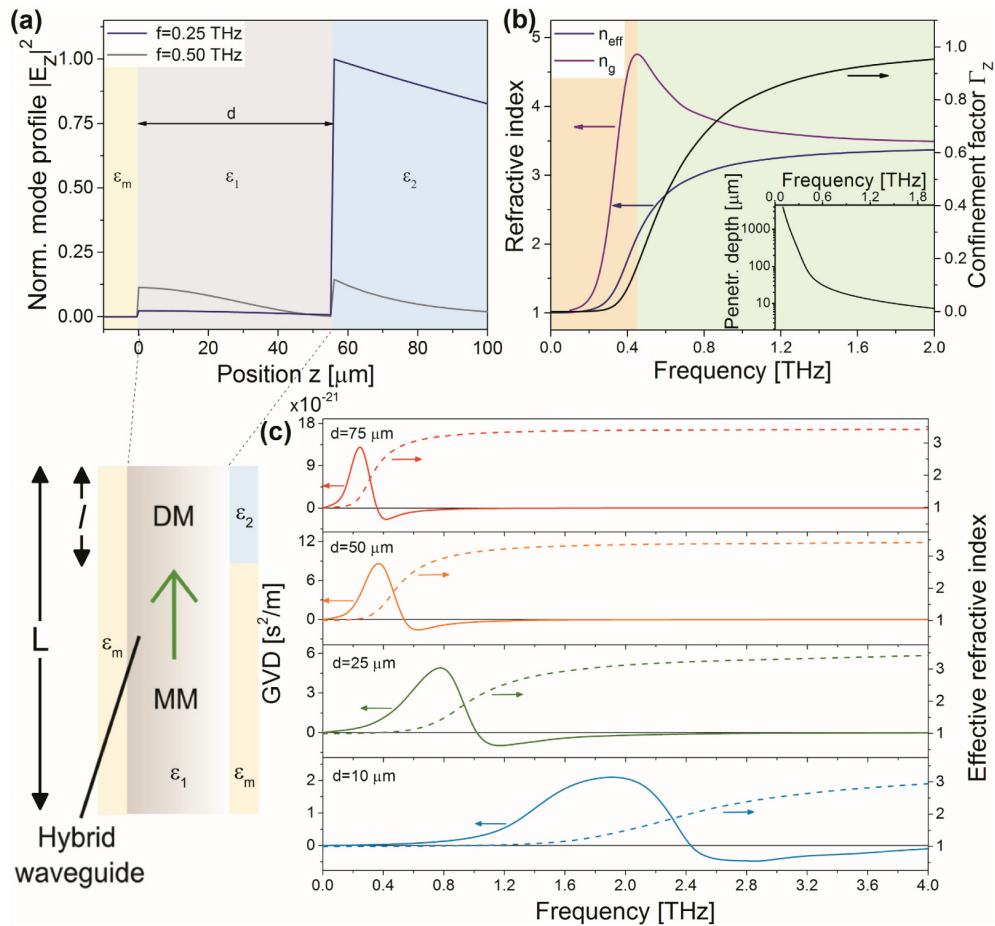


Fig. 1. (a) Mode profile of the absolute value of electric field in z -direction. The waveguide height is $d = 56 \mu\text{m}$ and the dielectric permittivities are set to $\epsilon_1 = 11.7$ (Si) and $\epsilon_2 = 1$ (air). (b) Frequency dependent penetration depth (inset), effective and group index (left axis) and confinement factor (right axis). The normal (orange) and anomalous (green) dispersion indicate positive and negative GVD, respectively. (c) Influence of waveguide height on both the dispersion relation (right axis, dashed curves) and GVD (left axis, bold curves). Interestingly, at typical QCL heights ($d = 10\text{--}20 \mu\text{m}$) the GVD zero crossing is at typical QCL frequencies (1.25–2.50 THz) offering broadband material and gain GVD compensation.

A hybrid waveguide is formed by integration of a DM section into a MM waveguide. At first, a theoretical model is employed to calculate the propagation constant of the fundamental TM_1 waveguide mode in the DM section. The model provides access to dispersion relation, penetration depth, confinement factor and most importantly the GVD.

In Fig. 1(a) the predicted transverse mode distribution is displayed including the three different regions of the DM section consisting of a gold, a silicon and an air-layer, for a frequency of 0.25 THz and 0.5 THz, respectively. The discontinuity of the electric field at the core-cladding interface is attributed to the different dielectric permittivity. As shown in in Fig. 1(b), lower frequencies provide a higher penetration depth into the outer dielectric and a lower confinement factor. This fact is also reflected in the dispersion relation in Fig. 1(b) where the effective refractive index n_{eff} approaches $n_{\text{air}} = 1$ for low frequencies and $n_{\text{Si}} = 3.42$ for high frequencies. By investigation of the group index n_g in Fig. 1(b) two regimes, one normal (orange) and one anomalous (green) regime, are identified indicating positive and negative GVD, respectively. In order to show that a waveguide height change is associated

with a shift of the dispersion properties with respect to frequency, both the GVD and the dispersion relation are shown in Fig. 1(c) for different waveguide heights. For example at a waveguide height of $d = 25 \mu\text{m}$, the GVD is negative at 1 THz, takes its minimum value of $-10^{-21} \text{ s}^2/\text{m}$ at 1.2 THz and reaches $-10^{-23} \text{ s}^2/\text{m}$ at 2.5 THz, which corresponds to more than an octave-spanning negative GVD regime. At THz frequencies, typical values of the positive GaAs material GVD are in the order of $-10^{-23} \text{ s}^2/\text{m}$ [27]. Also a strong broadband positive GVD regime is present at lower frequencies. For all waveguide heights presented in Fig. 1(c), it can be seen that large changes in the GVD occur when both the dispersion relation and the confinement factor (see Fig. 1(b)) change rapidly.

3.2 Experimental measurement: GVD and chirp analysis

Both a reference MM and a hybrid waveguide are cleaved into $L = 3.5 \text{ mm}$ long and 2 mm wide pieces. In order to experimentally access the dispersion and thereby the GVD features of the DM waveguide section a THz time domain spectroscopy setup is employed [35,36]. According to Fig. 2(a), THz radiation generated from an inter-digitated photoconductive antenna is coupled into a waveguide with a DM section of length l and a MM section of length $L-l$.

The signal is recorded electro-optically, which allows both time and frequency domain analysis. Fig. 2(b) shows the obtained electric field dynamics for the reference, a MM waveguide, and a hybrid waveguide with a $l = 336 \mu\text{m}$ long DM section. At a time of approximately 2 ps , a leakage of the THz pulse at the input facet is present. The leakage pulse amplitude is kept as small as possible using an Au-coated blocker. The high frequency signal occurs at a time of approximately 30 ps , which corresponds to the expected time delay

$$\Delta t = \frac{(n_{\text{Si}} - n_{\text{air}})L}{c} = 28 \text{ ps.}$$

To obtain the dispersion relation, a Fourier-transform of the time domain signal is taken followed by an extraction of the unwrapped spectral phase, $\phi(\omega)$. By taking into account the individual contributions according to the MM section of length $L-l$ and the DM section of length l , the pure spectral phase and hence the dispersion relation of the DM section is obtained (see section 2.2 for more details).

The experimental results for a waveguide height of $d = 40 \mu\text{m}$ are presented in Fig. 2(d) and are in good agreement with the theoretical model. The corresponding calculated GVD is depicted in the inset of Fig. 2(d) and shows a maximum GVD of $6.4 \times 10^{-21} \text{ s}^2/\text{m}$ at 0.5 THz and a minimum GVD of $-1.3 \times 10^{-21} \text{ s}^2/\text{m}$ at 0.8 THz .

In order to investigate the dispersive effects in time, the length of the DM section is increased to 2.3 mm to enhance the contribution of the DM section and clearly see any chirp. The GVD is mapped into the time domain by up- and down chirping the incoming THz signal. Figure 3(a) shows the resulting time domain signal, where the high frequency components are again localized at approximately 30 ps . Although most spectral intensity is present around 1 THz (see Wigner-Ville distribution (WVD)), some low frequency components are observed at previous times. This effect is even more pronounced when an optical low-pass THz filter that cuts off all frequencies above 1 THz is introduced into the setup. Although the utilized low-pass filter adds significant losses on the order of $10 - 50\%$ for frequencies below 1 THz , the low signal to noise ratio is mainly attributed to the challenging in-coupling for low frequencies. Low frequencies provide a large spot size, while high frequencies provide a smaller spot size with respect to the waveguide height. This explains the higher signal for higher frequencies. The fact that the leading part of the signal includes the low frequency components is in accordance with the dispersion relation (see Figs. 1(b)-1(c)), since lower frequencies are expected to travel faster.

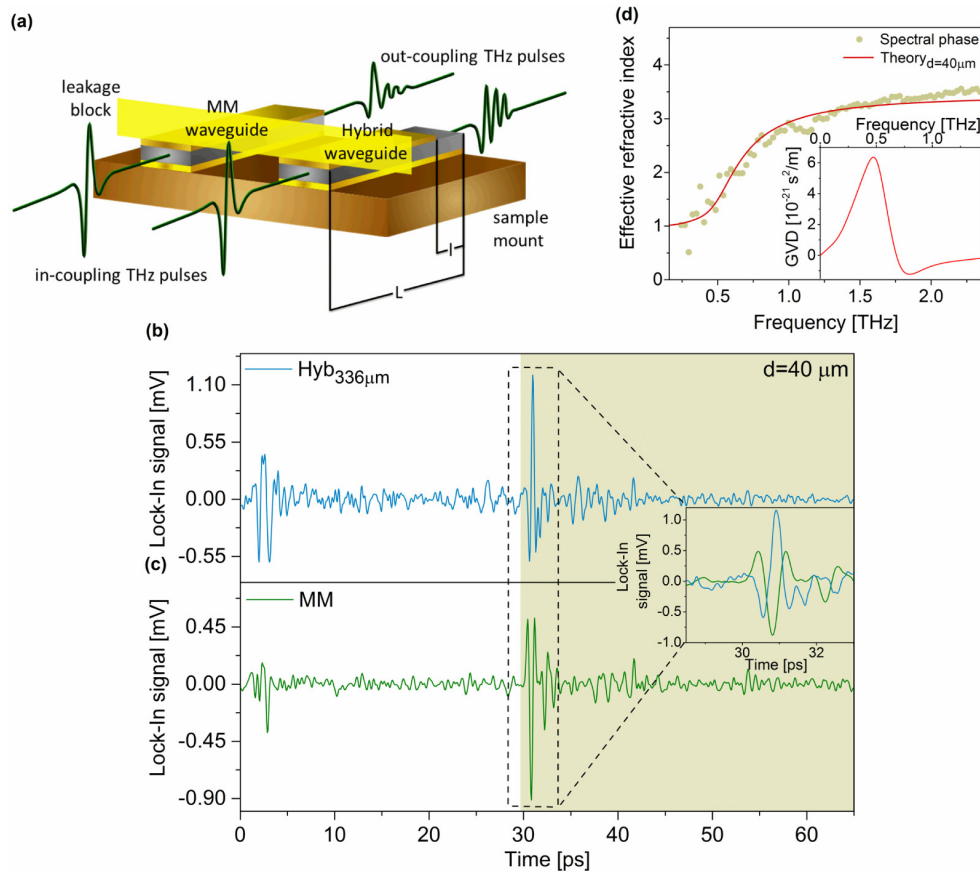


Fig. 2. (a) Schematic of the experimental geometry including an Au-coated leakage blocker (yellow) and the waveguides for an experimental determination of the dispersion relation via THz time domain spectroscopy for a waveguide height of $d = 40 \mu\text{m}$. (b) Time domain signal for a 3.5 mm long hybrid waveguide (blue) with a $l = 336 \mu\text{m}$ long DM section at the end of the ridge. (c) Time domain signal for a 3.5 mm long metal-metal (MM) waveguide (green). A minimized leakage at around 2 ps at the in-coupling facet is an essential factor for obtaining an accurate dispersion relation. The close-up illustrates the difference between both signals. The champagne-colored area corresponds to the time domain window that is used for the Fourier-transform and the spectral phase analysis. (d) Dispersion relation obtained from the spectral phase analysis (champagne circles) and the theoretical model (red line). The corresponding GVD is shown in the inset.

Additionally, the chirp is analyzed separately for both the high and low frequency components with respect to the instantaneous frequency in Figs. 3(c)-3(d) and Fig. 5. The instantaneous frequency is obtained by manually calculating the period at a given time. As shown in Fig. 3(c), the instantaneous frequency for the low frequency components is increasing (positive GVD), whereas in Fig. 3(d) the instantaneous frequency for the high frequency components is decreasing (negative GVD). In other words, the GVD is explicitly mapped into the time domain and indicates the large THz pulse shaping potential of the proposed hybrid waveguide. The measured dispersion relation calculated from the spectral phase from the Fourier-transform of the THz signal in Fig. 3(a) (purple region) is in good agreement with the theoretical dispersion relation shown in Fig. 3(e). The resulting GVD curve is presented in Fig. 3(f) and shows with respect to Fig. 2(d) both a blue-shift and a more pronounced GVD. This fact is attributed to the increased waveguide height, which is consistent with Fig. 1(c).

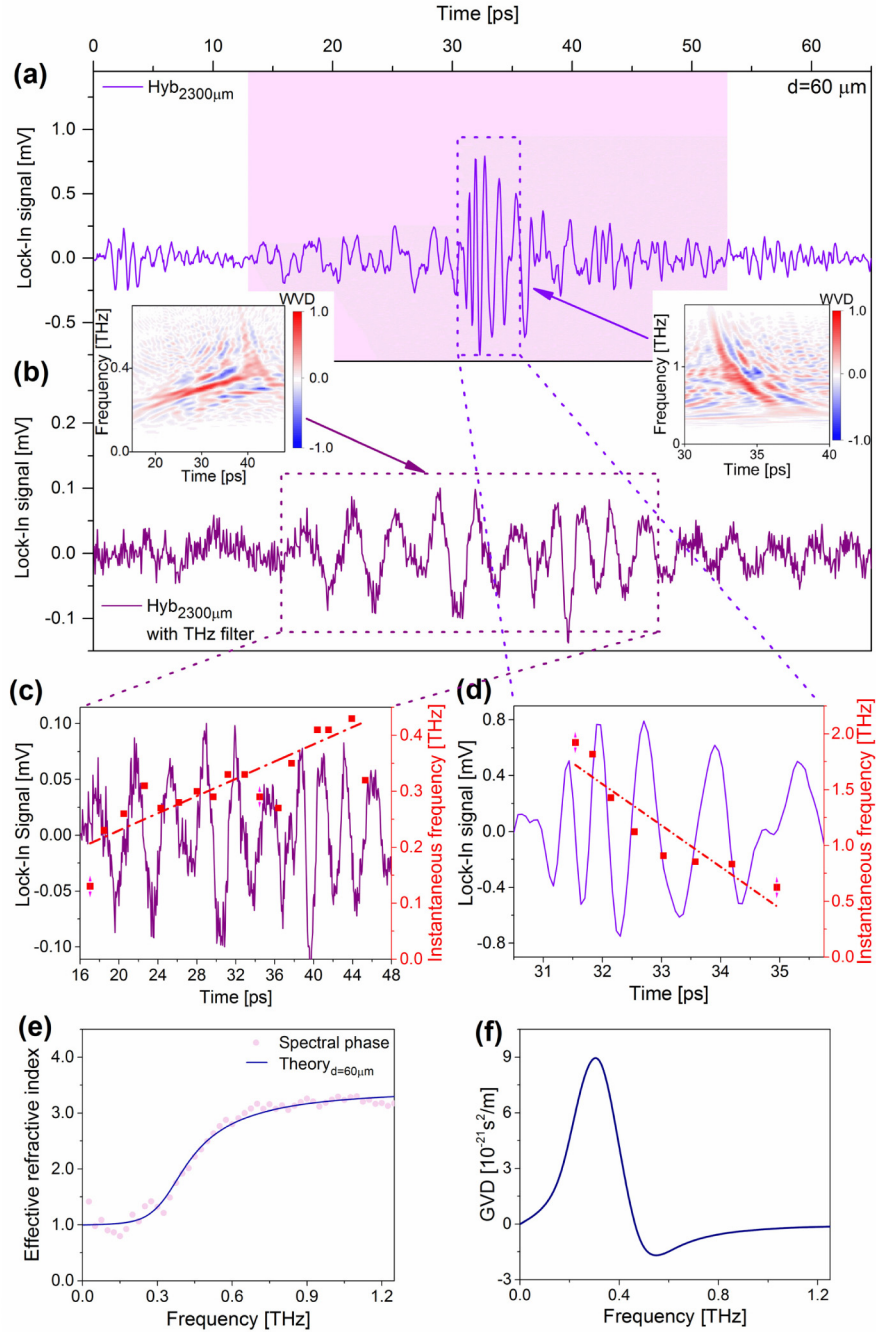


Fig. 3. (a) Time domain signal and Wigner-Ville distribution (WVD) based time-frequency domain analysis for a 3.5 mm long hybrid waveguide (violet) with a $L = 2.3$ mm long DM section and a waveguide height of $d = 60 \mu\text{m}$. (b) Repeated measurement as in Fig. 3(a) employing an optical low-pass THz filter that cuts off all frequencies above 1 THz (dark purple). (c) The increasing instantaneous frequency (positive chirp) reflects the positive GVD. (d) The decreasing instantaneous frequency (negative chirp) maps the negative GVD into the time domain. (e) Dispersion relation obtained from a Fourier-transform of the signal corresponding to the light purple area in Fig. 3(a) compared to the theoretical curve (blue). (f) GVD of the investigated hybrid waveguide as deduced from Fig. 3(e) (blue).

3.3 Simulation: material GVD compensation

The suitability of the hybrid waveguide for GVD compensation is examined by performing numerical GVD calculations. Besides the demonstrated GVD shifting in Fig. 1(c), the GVD can be tuned substantially by varying the top dielectric as shown in Fig. 4(a). Reducing the index contrast between the top dielectric and the waveguide core leads to both a reduction of the GVD and its curvature. This fact can be used to improve the flatness of the GVD curve and is called GVD-flattening. For example, the GVD curve of a composite hybrid waveguide with two DM sections with different top dielectric materials ($n_{2,1} = 1.54$ and $n_{2,2} = 2$) is shown in Fig. 4(b). The two DM sections are 16% and 40% of the total laser ridge length, respectively. The residual 44% of the length is kept as a MM waveguide. The composite hybrid waveguide GVD (black) compensates for the material GVD (blue) over a broad range of almost 1 THz as shown by the turquoise line in Fig. 4(b). In contrast, the waveguide GVD for a $d = 13 \mu\text{m}$ thick MM waveguide (grey) (adapted from [28]) is shown in Fig. 4(b). The MM waveguide GVD is close to zero and does not offer significant GVD tuning.

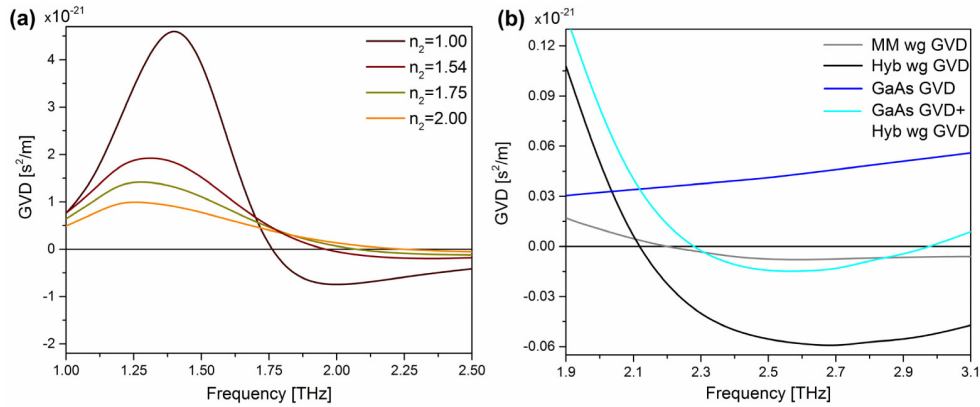


Fig. 4. (a) DM section waveguide GVD for different top dielectrics and a waveguide height of $d = 13 \mu\text{m}$ demonstrating a GVD-flattening. (b) GaAs material GVD (blue), MM waveguide GVD (grey) [28] and hybrid waveguide GVD (black). For GVD compensation, a composite hybrid waveguide with two different top dielectric materials with $n_{2,1} = 1.54$ and $n_{2,2} = 2$ is used. The DM section lengths correspond to 16% and 40% of the ridge length, respectively. The broad hybrid waveguide GVD allows a broad material GVD compensation (turquoise).

4. Wigner-Ville distribution based chirp analysis

In 1932, E. Wigner found a distribution function in the context of statistical quantum mechanics [37], which, in 1948, has been extended by J. Ville to the field of signal processing [38]. The resulting so-called time and frequency dependent Wigner-Ville distribution (WVD) for a signal $E(t)$ is defined as [39]

$$W(t, f) = \frac{1}{2\pi} \int_{-\infty}^{\infty} s(t - \frac{\tau}{2}) s^*(t + \frac{\tau}{2}) \exp(-i2\pi\tau f) d\tau, \quad (8)$$

where $s(t)$ is the analytical signal associated to the real-valued time-domain signal $E(t)$ via a

Hilbert-transform $H[E(t)] = \frac{1}{\pi} \int_{-\infty}^{\infty} \frac{E(p)}{t - p} dp$ in the following way:

$$s(t) = E(t) + iH[E(t)]. \quad (9)$$

The WVD is a highly non-local time-frequency representation of a signal, since it measures the correlation of a signal $s(t)$ at previous and future times, respectively. Since both far and close times contribute equally, the non-local character becomes obvious and leads to the

following implications: The WVD at time t might show noisy behavior even though the signal $s(t)$ is smooth. Similarly, the WVD at time t might be unequal to zero even though the signal $s(t)$ is zero. Besides these implications, the WVD has the advantageous property that via its first conditional moments with respect to frequency and time the instantaneous frequency and the group delay, respectively, can be calculated. Also the WVD is an illustrative time-frequency representation that makes use of two-dimensional time-frequency matrices. In this section, the WVD is employed to perform a time-frequency analysis of the obtained time domain spectroscopy signals. More precisely, the WVD is used to investigate the chirp of the hybrid waveguide signals shown in Figs. 3(a)-3(b) with respect to both chirp and instantaneous frequency. In order to determine the instantaneous frequency, the time-frequency marginal of the WVD is introduced:

$$\int_{-\infty}^{\infty} W(t, f) df = |s(t)|^2. \quad (10)$$

Then, the instantaneous frequency (IF) is given by the first conditional moment with respect to frequency:

$$IF(t) = \frac{1}{|s(t)|^2} \int_{-\infty}^{\infty} f \cdot W(t, f) df. \quad (11)$$

Before the WVD and the instantaneous frequency are determined for the experimental signal, as an illustrative example, the WVD for an ideally chirped input signal is calculated analytically. More concretely, the WVD for a signal $s(t) = \exp(i2\pi bt^2)$ ($b = \text{const.}$) that provides a linear instantaneous frequency $IF(t) = 2bt$ is given by:

$$W_{ch}(t, f) = \int_{-\infty}^{\infty} \exp\left(-i2\pi b\left(t - \frac{\tau}{2}\right)^2\right) \exp\left(i2\pi b\left(t + \frac{\tau}{2}\right)^2\right) \exp(-i2\pi\tau f) d\tau = \delta(f - 2bt). \quad (12)$$

This implies that the WVD of a chirped signal $W_{ch}(t, f)$ is a line in the time-frequency space, where the slope b correlates with the GVD. For a Gaussian function $\exp(-l(t-t_0)^2)$ with $l = \text{const.}$ and $t_0 = \text{const.}$, the WVD, $W_G(t, f)$ is proportional to a Gaussian again

$$W_G(t, f) \sim \exp(-m(t-t_0)^2 - nf^2), \quad (13)$$

where $n = \text{const.}$. Ultimately, the WVD is calculated for a signal with a Gaussian envelope and a chirped carrier. For a separable function $y(t) = x(t)h(t)$ the multiplication theorem of the WVD allows to write for a y -dependent WVD, $W_y(t, f)$:

$$W_y(t, f) = \int_{-\infty}^{\infty} W_x(t, \rho) W_h(t, f - \rho) d\rho. \quad (14)$$

Employing the practical property of the delta distribution $f(a) = \int_{-\infty}^{\infty} f(x)\delta(a-x)dx$ with $a = \text{const.}$, the final WVD for a Gaussian envelope and a chirped carrier, $W_{ch,G}(t, f)$ takes the form:

$$W_{ch,G}(t, f) = \int_{-\infty}^{\infty} W_{ch}(t, \rho) W_G(t, f - \rho) d\rho \sim \exp(-m(t-t_0)^2 - n(f-2bt)^2). \quad (15)$$

The WVD for an un-chirped Gaussian signal is visualized in Fig. 5. As expected, the corresponding instantaneous frequency is a constant given by the arbitrarily chosen carrier frequency of 0.5 THz. Incorporating a negative or a positive chirp, i.e. $b = -0.05 \text{ ps}^{-2}$ or $b =$

0.05 ps^{-2} , respectively, the resulting WVD is concentrated along the instantaneous frequency, which is in accordance with the analytical prediction reflected by Eq. (15). As depicted in Figs. 5(b,c), the corresponding IF for the negative chirp decreases linearly and features a linear increase for a positive chirp, respectively.

Using the experimental signal from Fig. 3(a), the obtained WVD shown Fig. 5(d) exhibits an analogy with respect to Fig. 5(b) and the analytically predicted WVD (Eq. (15)). This reflects the negative chirp of the hybrid waveguide for high frequencies. Accordingly, the IF approximately features a linear decrease. The approach presented in Fig. 3(d), where the IF is obtained by taking the inverse of the individual oscillation periods in time at a center time is shown in Fig. 5(d) to be in good agreement with the WVD based approach. Similarly, as shown in Fig. 5(e) for low frequencies, the positive hybrid waveguide GVD is mapped into both the WVD and the IF curve. Again, both approaches to obtain the IF are in good agreement. However, due to the fact that for the low frequency case the signal to noise ratio is intrinsically worse compared to the high frequency case – reflected by the grey curve in Fig. 5(d) - a running average (50 points) is employed to still extract the positive chirp in agreement with Fig. 3(c) reflected by the black curve in Fig. 5(e). The discontinuous background in Fig. 5(d,e) is attributed to the periodically repeating antenna leakage signal, thus perturbing the non-local WVD. In contrast, in Fig. 5(a-c) there is no leakage, which prevents any formation of discontinuities.

Qualitative deviations between both the calculated Gaussian WVD and the experimental WVD are attributed to the fact that the experimental input THz signal does not constitute a perfect Gaussian pulse. Mathematically it can be shown that the WVD is only non-negative for Gaussian shaped pulses. Remarkably, the WVD is always positive for a Gaussian input signal. In contrast, for THz pulses, the carrier envelope approximation is no longer valid. Furthermore, higher order dispersive effects, such as third-order dispersion of the hybrid waveguide affect the results, too. Finally, a leakage of the input signal that is not coupled into the hybrid waveguide that is particularly relevant for low frequencies might perturb the WVD and thus the IF curve, too. However, the WVD time-frequency analysis clearly supports the GVD features of the proposed hybrid waveguide and represents an illustrative tool towards signal analysis by providing more illustrative insights than a classical spectrogram.

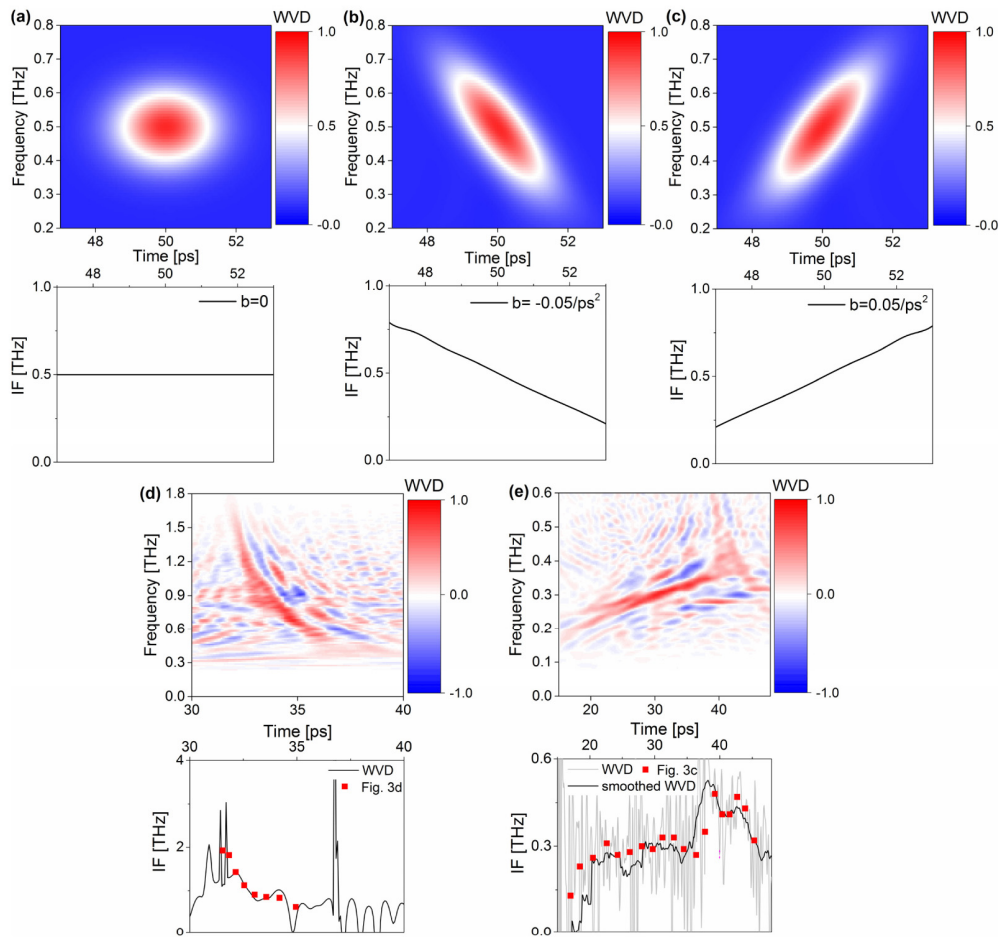


Fig. 5. (a) WVD of an un-chirped Gaussian pulse (numerical example) and constant instantaneous frequency (IF) (black curve). (b) Negatively chirped Gaussian pulse with linearly decreasing IF. (c) Positively chirped Gaussian pulse with linearly increasing IF. (d) Negatively chirped hybrid waveguide signal from Fig. 3(a) pulse with an approximately linear decrease of the IF. The IF data from Fig. 3(d) (red squares) is in good accordance with the IF obtained from the WVD (black curve). (e) Positively chirped hybrid waveguide signal from Fig. 3(b) with an approximately linear increase of the IF. The IF data from Fig. 3(c) (red squares) is compared to the IF obtained from the WVD (black curve: smoothed IF, grey: unsmoothed IF).

5. Discussion

A broadband THz dispersion control by integration of a DM section into a MM waveguide is successfully demonstrated. By removing one metal-dielectric boundary, the waveguide mode significantly resides both into the high refractive index core and the dielectric cladding of low refractive index. By these simple modifications to a regular MM waveguide a hybrid waveguide is formed whose effective refractive index lies between the index of the core ($n_{Si} = 3.42$) for high frequencies and the index of the top dielectric ($n_{air} = 1$) for low frequencies. By tuning the waveguide height between $d = 10 \mu\text{m}$ and $d = 75 \mu\text{m}$, we numerically demonstrate in Fig. 1(c) that the DM section provides broadband positive and negative GVD on the order of $10^{-21} \text{ s}^2/\text{m}$ ranging from 0 to 3 THz. Interestingly, at typical THz quantum cascade laser (QCL) [40,41] MM waveguide heights (approximately $d = 10 \mu\text{m}$), strong broadband negative GVD on the order of $-10^{-21} \text{ s}^2/\text{m}$ and $-10^{-22} \text{ s}^2/\text{m}$ is featured, which is present at

typical THz QCL frequencies (2-4 THz). This fact stresses the appeal of the hybrid waveguide for QCL applications. In addition, a strong broadband positive GVD regime is present at lower frequencies offering a compensation of two contrary GVD contributions simultaneously present at different frequencies such as negative gain and positive material GVD. As a further potential application, the presented concept could help to improve the dispersion control in THz fibres [42,43], which could enable THz self-phase modulation based on slow light effects. Summarizing the GVD tuning of the hybrid waveguide, GVD-shifting is predominantly achieved by changing the waveguide height, whereas GVD-flattening is obtained by reducing the index contrast between the core and the cladding shown in Fig. 4(b). Further research could be devoted to an expansion of the dispersion control by engineering the top dielectric shape or properties.

By employing THz time domain spectroscopy, we obtained both qualitative and quantitative experimental assessment of the dispersion relation and hence the GVD. On the one hand, the experimental dispersion relation is quantitatively extracted from the spectral phase obtained from a Fourier-transform of the MM and hybrid waveguide time domain signals. For both investigated hybrid waveguides the experimentally obtained dispersion relations are in good accordance with the theoretical model. On the other hand, the GVD is mapped into the time domain by up- and down- chirping the in-coming THz signal. Analyzing the chirp for a long DM section, both a positive chirp for low frequencies (positive GVD) and negative chirp for high frequencies (negative GVD) are individually observed. The calculated WVD is concentrated along the instantaneous frequency. The performed measurements show both the large THz pulse shape and pulse compression potential of the hybrid waveguide. For example, this could lead to an improved signal to noise ratio for THz detection by compressing chirped THz signals or to ultra-short and broadband THz pulses. The input parameters of the introduced theoretical model are the waveguide height and the dielectric functions of the underlying three layer system (Eq. (6)). The numerical results for a specifically designed hybrid waveguide show a broadband compensation of positive GaAs material GVD (Fig. 4(b)). From the application point of view, dispersion compensation based on the presented hybrid waveguide is straight-forward due to the manageable theoretical, numerical and experimental effort. Consequently, the hybrid waveguide concept can be considered not only as more broadband but also as more user-friendly – especially when compared to Gires-Tournois interferometers [23] or the design of chirped mirrors [27], which are both fundamentally different from the presented hybrid waveguide. Also the proposed hybrid waveguide could offers great potential for broadband gain GVD compensation, which is a key factor for THz frequency comb applications [28].

6. Conclusion

In conclusion, we have demonstrated that a novel DM waveguide mode section integrated into a common MM waveguide features strong broadband positive and negative GVD in the THz regime, thus providing THz dispersion control. Experimental evidence is obtained both in time and frequency domain for two samples of different waveguide heights. A Wigner-Ville study of the experimental data completes the GVD analysis and reveals the attractiveness of the Wigner-Ville distribution concept for chirp analysis including instantaneous frequency calculations. Positive and negative chirp are individually observed and identified with positive and negative GVD, respectively. In addition, we have numerically indicated that positive material GVD from GaAs can be compensated from 2.2 THz to 3.1 THz using a composite hybrid waveguide of a typical QCL height of 13 μm . Remarkably, the fact that the proposed waveguide provides substantial broadband positive and negative GVD at both, typical QCL heights and frequencies, defines a natural suitability for QCL applications, such as the compensation of material and gain GVD for THz applications. Further interesting applications including THz fibres, THz solitons, THz pulse compression and THz self-phase modulation based on slow light generation stress the broad

potential of the proposed waveguide. Finally, the presented hybrid waveguide is user friendly, and could be used for both intra- and extra cavity applications.

Acknowledgment

T.F, S.P, N.J., and A.D.W. would like to acknowledge IMPRS-SurMat and MPIE Düsseldorf. T.F., S.M., and N.J. would like to acknowledge DFG GSC 98/3 RUB Research School PLUS. Additionally, P.B. acknowledges support by the Cluster of Excellence RESOLV (EXC1069) funded by the Deutsche Forschungsgemeinschaft. We acknowledge support by the Open Access Publication Funds of the Ruhr-Universität Bochum.